Frontal dynamics of powder snow avalanches Supplementary online material

C. S. Carroll,[1] M. Y. Louge,[1] and B. Turnbull[2]

1. Supplementary Appendices

This document contains a nomenclature, as well as Appendices A-H with calculations and discussions in support of "Frontal dynamics of powder snow avalanches".

Appendix A: Cloud velocity and static pressure fields

In the avalanche rest frame, the RHB velocity field below the interface derives from the stream function

$$\psi = U'(-r\sin\theta + b'\theta), \tag{A1}$$

where $0 \leqslant \psi < \pi U' b'$ and (r,θ) are polar coordinates about the source with angle θ counted from the $\hat{\mathbf{x}}$ unit vector pointing from source to stagnation (Fig. 1). The curvilinear coordinate s on a streamline ψ with origin at the source is such that

$$\frac{\mathrm{d}s}{b'\mathrm{d}\theta} = \frac{\sqrt{(\psi^*-\theta)^2 + [1+(\psi^*-\theta)\cot\theta]^2}}{\sin\theta}, \tag{A2}$$

where $\psi^* \equiv \psi/(U'b')$ is the dimensionless streamfunction. The resulting velocity field is

$$\begin{aligned} u'_r &= \frac{1}{r}\frac{\partial\psi}{\partial\theta} = U'(-\cos\theta + b'/r) \\ u'_\theta &= -\frac{\partial\psi}{\partial r} = U'\sin\theta \end{aligned} \tag{A3}$$

in radial and azimuthal directions, respectively, or

$$\mathbf{u}' = U'\left[\frac{xb'}{(x^2+y^2)} - 1\right]\hat{\mathbf{x}} + U'\left[\frac{yb'}{(x^2+y^2)}\right]\hat{\mathbf{y}} \tag{A4}$$

in cartesian coordinates (x,y) along $\hat{\mathbf{x}}$ and the outward unit vector $\hat{\mathbf{y}}$ normal to the snowpack surface. (This velocity field becomes $\mathbf{u}' + U\hat{\mathbf{x}}$ in the mountain frame of reference). Invoking Bernoulli's Eqs. in ambient air and cloud, considering flow to be quasi-steady, and matching static pressure at the interface, *Carroll et al.* [2012] calculated the pressure field within the cloud as

$$p' = p_\infty + p_z + \bar{p} + p_u, \tag{A5}$$

where z is altitude from the current position of the stagnation point, p_∞ is a reference atmospheric air pressure at $z=0$,

$$p_z \equiv -\rho' g z, \tag{A6}$$

$$\bar{p} \equiv \frac{\rho}{2}U^2 - \frac{\rho'}{2}U'^2 = \frac{\rho}{2}U^2\left(\frac{\mathrm{Ri}}{1+\mathrm{Ri}}\right), \tag{A7}$$

and p_u is the flow-induced part of static pressure in the powder cloud,

$$\frac{p_u}{(\rho'/2)U'^2} = \frac{2xb' - b'^2}{x^2+y^2} = \frac{b'}{r}\left(2\cos\theta - \frac{b'}{r}\right). \tag{A8}$$

Appendix B: Size of the frontal region

On any streamline ψ in Eq. (A1) below the interface, the flow-induced pressure p_u in the source fluid is

$$p_{u_s}(\psi) = \frac{\rho'}{2}U'^2\frac{\sin\theta}{(\theta-\psi^*)}\left(2\cos\theta - \frac{\sin\theta}{\theta-\psi^*}\right). \tag{B1}$$

Its gradient along a streamline is "favorable" $(\partial p_{u_s}/\partial s) < 0$ for $y > b' - x$, and "adverse" $(\partial p_{u_s}/\partial s) > 0$ for $y < b' - x$. On the interface where $\psi = 0$ and $r = b'\theta/\sin\theta$, $p_{u_s}(\psi = 0)$ vanishes at $x = b'/2$ ahead of the source ($\theta \simeq 10\pi/27$), and is always < 0 downstream of that point. Because the interface has favorable pressure gradient until $\theta = \theta_f \simeq 13\pi/20$, and adverse $\forall\theta > \theta_f$, it is convenient to define the frontal region as bounded by the exit plane where $\partial p_{u_s}/\partial s = 0$ or, equivalently, as the region $x > x_f$ with

$$x_f = b'\theta_f/\tan\theta_f < 0. \tag{B2}$$

With interface described by $x = b'\theta/\tan\theta$ and $y = b'\theta$, the volume V of the frontal region is obtained by changing variable from x to θ and integrating,

$$V = -b'^2 W\int_{\theta=0}^{\theta_f}\theta\Big[\frac{1}{\tan\theta} - \frac{\theta}{\sin^2\theta}\Big]\mathrm{d}\theta. \tag{B3}$$

Using Jonquière's polylogarithm function $\mathrm{Li}_n(\epsilon)$ of the complex argument ϵ, we find

$$\begin{aligned} V = \frac{b'^2 W}{12}\imath\Big[\pi^2 + 12\imath\theta_f\Big(\frac{\theta_f}{\tan\theta_f} - \ln(1-e^{2\imath\theta_f})\Big) \\ -6\mathrm{Li}_2(e^{2\imath\theta_f}) - 6\theta_f^2\Big] \equiv a_V b'^2 W, \end{aligned} \tag{B4}$$

where $\imath^2 = -1$. At θ_f, we calculate $a_V \simeq 3.00$.

Appendix C: Quasi-steady approximation

For any streamline within the frontal region ($0 \leqslant \psi^* < \pi$), the residence time from the source ($\theta = \psi^*$) to any arbitrary point on the streamline at $\theta = \theta_t$ is

$$\begin{aligned} \tau_R(\psi^*,\theta_t) &= \int_{\theta=\psi^*}^{\theta_t}\frac{\mathrm{d}s}{\mathrm{d}\theta}\frac{\mathrm{d}\theta}{\|\mathbf{u}\|} \\ &= (b'/U')\left[\ln(\sin\theta_t/\sin\psi^*) - (\theta_t-\psi^*)/\tan\theta_t\right], \end{aligned} \tag{C1}$$

where $\|\mathbf{u}'\|$ is the velocity magnitude from Eq. (A3), and $ds/d\theta$ is given by Eq. (A2). Then, the mean residence time of a particle from source to exit plane is

$$\bar{\tau}_R = \frac{1}{\pi}\int_{\psi^*=0}^{\pi}\tau_R(\psi^*,\theta_t)\mathrm{d}\psi^* \equiv a_R(b'/U'), \tag{C2}$$

[1]Sibley School of Mechanical and Aerospace Engineering, Cornell University, Ithaca, NY 14853, USA.

[2]Division of Process and Environmental Engineering, University of Nottingham, UK.

0148-0227/13/$9.00

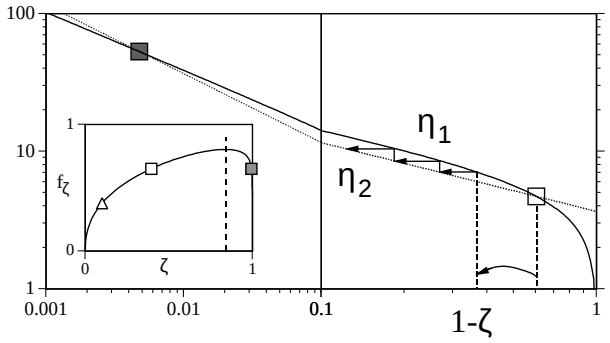

Figure 1. η_1 and η_2 vs. $(1-\zeta)$ for $\mathrm{Ri} = \mathrm{Ri}_n$, $\lambda \simeq 14\%$ and $\chi_0 \simeq 8.4$, corresponding, for example, to $\rho_c = 100\,\mathrm{kg/m^3}$, $\rho = 1.2\,\mathrm{kg/m^3}$, $\alpha = 30\,^\circ$, and $\mu_e = 0.45$. Because the two curves are very close, we plot them vs. $(1-\zeta)$ and we magnify the range $0.1 < (1-\zeta) < 1$ around the unstable solution. Inset: f_ζ vs. ζ. The dashed line marks the peak at $\zeta = \zeta_n = 2a_1$. Symbols correspond to solutions of Eq. (D5) shown in Fig. (2) of the paper.

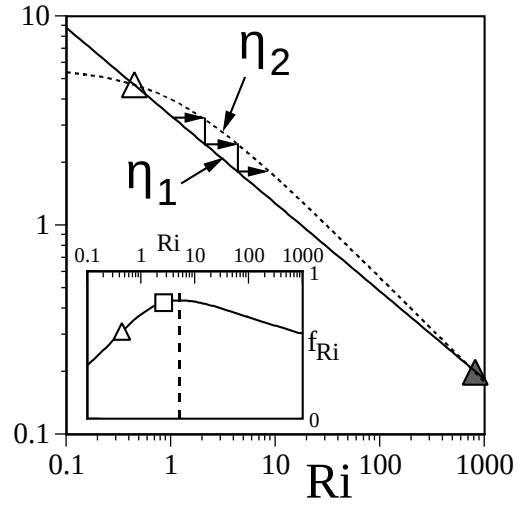

Figure 2. η_1 and η_2 vs. Ri for $(1-\zeta) = 0.1$, $\lambda \simeq 19\%$, and $\chi_0 \simeq 8.4$. Inset: f_{Ri} vs. Ri. The dashed line marks the peak at $\mathrm{Ri} = \mathrm{Ri}_n = 2a_1/(1-2a_1)$. Symbols, see Fig. 1.

where $\theta_t(\psi^*)$ is the polar angle of the intersection of dimensionless streamline ψ^* with the exit face at θ_f. We calculate $a_R \simeq 0.956$.

Turnbull and McElwaine [2007] noted that total avalanche volume $\mathbb{V}_T$ was proportional to the cube of time t from release or, equivalently, $d\ln\mathbb{V}_T \sim 3\mathrm{d}\ln t$ [*Vallet et al.*, 2004]. With uniform slope and width, volume of the frontal region and total volume are roughly proportional, $\mathrm{d}\ln V \sim \mathrm{d}\ln\mathbb{V}_T$. Then, using $\mathrm{d}\ln b' = (1/2)\mathrm{d}\ln V$, we deduce the characteristic time for cloud growth $\bar\tau_G \sim b'/(\mathrm{d}b'/\mathrm{d}t) = (\mathrm{d}\ln b'/\mathrm{d}t)^{-1} \sim (2/3)t$. Therefore, growth takes longer than the residence time ($\bar\tau_G > \bar\tau_R$) after

$$t > (3a_R/2)(b'/U'). \tag{C3}$$

Beyond such time, which is typically $\sim 1\,\mathrm{s}$, the size of the control volume around the frontal region may be regarded as "quasi-steady" to establish mass and momentum balances (Fig. 1).

To preserve symmetry and derive Eq. (1) analytically, *Carroll et al.* [2012] restricted attention to horizontal flows. For us to generalize their results to an inclined suspension, the streamwise component $(g\sin\alpha)$ of gravity on a slope of inclination α must produce a particle displacement along $\hat{\mathbf{x}}$ during the mean residence time $\bar\tau_R$ from source to exit plane that is negligible compared to H', i.e.

$$(1/2)g\sin\alpha\bar\tau_R^2 \ll H'. \tag{C4}$$

Combining Eqs. (4), (5), (24) and (C2), criterion (C4) may be written

$$\sin\alpha \ll 4\pi^2(1-2a_1)/a_R^2 \simeq 6.9, \tag{C5}$$

which is upheld for any slope or conditions.

Appendix D: Stability

We define the quantities η_1 and η_2 proportional to h'/b'

$$\eta_1 \equiv \frac{\chi_0}{\mathrm{Ri}^{a_1}}\Big(\frac{\zeta}{1-\zeta}\Big)^{a_1}, \tag{D1}$$

where χ_0 is defined in Eq. (21) and

$$\eta_2 \equiv \frac{1}{\lambda\sqrt{(1+\mathrm{Ri})(1-\zeta)}}. \tag{D2}$$

Solutions of Eq. (16) arise when λ, ζ and Ri are such that $\eta_1 = \eta_2$ or, equivalently, when the functions

$$f_\zeta \equiv \zeta^{a_1}(1-\zeta)^{\frac{1}{2}-a_1} \tag{D3}$$

and

$$f_{\mathrm{Ri}} \equiv \frac{\mathrm{Ri}^{a_1}}{\sqrt{1+\mathrm{Ri}}} \tag{D4}$$

satisfy

$$\lambda\chi_0 f_\zeta = f_{\mathrm{Ri}}. \tag{D5}$$

As insets in Figs. 1–2 show, f_{Ri} and f_ζ peak, respectively, at the bulk Richardson Ri_n in Eq. (17) and the relative density ζ_n in Eq. (18) where $f_\zeta = f_{\mathrm{Ri}} = (2a_1)^{a_1}(1-2a_1)^{\frac{1}{2}-a_1}$. Inspection of f_ζ and f_{Ri} reveals that Eq. (D5) has zero, one or two solutions. A single solution is possible when f_ζ and f_{Ri} peak simultaneously, whereby λ is fixed at the value λ_n quoted in Eq. (20). If two solutions exist, the following stability argument, similar to that invoked in the mass balance of well-stirred reactors [*Strehlow*, 1984], can determine to which solutions the avalanche naturally evolves. Although we present the argument graphically, it is equivalent to a linear stability analysis based upon small perturbations of frontal density or speed about steady solutions of the mass conservation equation $V\partial\rho'/\partial t = \dot m_s - \dot m_e$ [*Uppal et al.*, 1976].

First, we note that causality matters. η_1 represents the fluidized depth that an avalanche can produce. In other words, frontal operational parameters (Ri, ζ) set η_1,

$$(\mathrm{Ri},\zeta) \Rightarrow \eta_1. \tag{D6}$$

Conversely, η_2 determines the avalanche size that such fluidization engenders,

$$\eta_2 \Rightarrow (\mathrm{Ri},\zeta,\lambda). \tag{D7}$$

These relations imply that, of two possible solutions, the stable one has the largest Ri and/or ζ (solid symbols in Figs. 1 and 2). To show this, consider the solution at fixed

Ri and λ denoted by an open square in Fig. 1. Any small perturbation resulting in a lower $(1-\zeta)$ (illustrated by a curved arrow) produces a larger η_1. In turn, because the new value of $\eta_2 = \eta_1$ implies yet a lower $(1-\zeta)$, the state of the avalanche diverges away from the original solution. Similarly, any excursion to a higher $(1-\zeta)$ also strays away from the solution. Therefore, the solution is unstable. Conversely, the solid square in Fig. 1 marks a stable solution, to which the mass balance always returns despite small perturbations. A similar reasoning at fixed ζ and λ in Fig. 2 shows that the open triangle at low Ri is unstable, while its filled counterpart at higher Ri is stable.

In general, solutions with $\zeta < \zeta_n$ (low frontal density) *or* $\mathrm{Ri} < \mathrm{Ri}_n$ (small avalanche height) are unstable. Conversely, solutions with high frontal density ($\zeta > \zeta_n$) *and* tall avalanches ($\mathrm{Ri} > \mathrm{Ri}_n$) are stable. As in well-stirred reactors [*Strehlow*, 1984], "ignition" toward larger ζ or Ri occurs as soon as either Ri *or* ζ exceeds an unstable solution. If such ignition can be achieved, dynamics progressively raise ζ and Ri toward higher frontal density and size, until the avalanche reaches the solution with Richardson Ri_n and relative density ζ_n in Eqs. (17) and (18).

Appendix E: Force and momentum integrals

The first derivative term on the right of Eq. (31) is

$$\frac{\partial}{\partial t}\int_{V(t)} \rho' U \mathrm{d}V = a_V \frac{\partial}{\partial t}(\rho' U b'^2 W), \tag{E1}$$

where W is cloud width and a_V is calculated in Appendix A. (Note that, because $\lambda_n h_n'/H' = \rho/(\rho_c \cos\alpha) \ll 1$, we neglect any contribution from the scoured top layer of the snowpack to frontal volume or dynamics). In the avalanche frame, the overall momentum of the frontal region along $\hat{\mathbf{x}}$ is

$$\int_V \rho'(\mathbf{u}'\cdot\hat{\mathbf{x}})\mathrm{d}V = -a_M \rho' b'^2 W U'. \tag{E2}$$

Integrating Eq. (A4), the x-momentum in an infinitesimal section $\mathrm{d}x$ of the frontal region vanishes in front of the source $\forall x > 0$, but is equal to $-\pi\rho' U' b' W$ behind it, $\forall x < 0$. So, with $x_f < 0$,

$$a_M = \frac{1}{b'}\int_{x_f}^{b'} \pi \mathbb{H}(-x)\mathrm{d}x = -\frac{\pi\theta_f}{\tan\theta_f} \simeq 3.28. \tag{E3}$$

where the Heaviside function $\mathbb{H}$ equates unity for positive argument and vanishes otherwise. Because x-velocities exist in equal measure along $\pm\hat{\mathbf{x}}$ ahead of the source, the nose section with $0 < x < b'$ possesses no net x-momentum in the rest frame of the avalanche.

We now consider forces in Eq. (31). First, we dismiss the shear force per unit width exerted by the turbulent suspension on the surface of the snowpack within the frontal region. Assuming at worst a uniform turbulent shear stress $\rho' u_{\mathrm{shear}}^2$ over the entire snowpack length $b'(1-\theta_f/\tan\theta_f)$ below the frontal region, where $u_{\mathrm{shear}} \sim a_S U'$ is a shear velocity, basal shear is negligible compared to weight $(\rho' V g \sin\alpha)$ along $\hat{\mathbf{x}}$, as long as

$$\sin\alpha \gg 2\pi \frac{a_S^2}{a_V}(1-2a_1)\Big(1-\frac{\theta_f}{\tan\theta_f}\Big). \tag{E4}$$

We estimate a_S by approximating the flow from snowpack to interface as a turbulent boundary layer [*Kays et al.*, 2005], for which $1/a_S = U'/u_{\mathrm{shear}} \simeq 5.5 + 2.5\ln(H_n^+)$, where $H_n^+ = \rho_n' H_n' u_{\mathrm{shear}}/\mu_f$ is the "wall coordinate" of the interface and μ_f is the dynamic viscosity of air. Substituting Eqs. (24) and (30), we find $0.02 < a_S < 0.03$ for frontal speeds $10 < U < 60\,\mathrm{m/s}$. Substituting in criterion (E4), neglecting basal shear requires $\sin\alpha \gg 6.10^{-4}$, which is clearly satisfied over any typical slope.

Next, we consider the resistance $\mathbf{F}_\mu$ of ambient air to frontal acceleration, which acts as an added mass $\rho a_\mu b'^2 W$. Because the frontal region is part of a larger body of dense fluid, we estimate its share of added mass by noting that it closely resembles the quarter of a cylindrical ellipse with semi-minor axis $\theta_f b'$ in the y-direction,

$$\mathbf{F}_\mu \cdot \hat{\mathbf{x}} = -\rho a_\mu b'^2 W \frac{\mathrm{d}U}{\mathrm{d}t}, \tag{E5}$$

where $a_\mu \simeq \pi\theta_f^2/4$. Because $\mathbf{F}_\mu$ is proportional to frontal acceleration, we group it with rate expressions in Eqs. (E1)–(E2) to form the left-hand side of Eq. (33). The right-hand side of that Eq. is the resultant of all forces on the frontal region minus the momentum output through its surfaces. Next, we show that it vanishes in the potential theory.

Static pressure applied on all surfaces of the frontal region, collectively called S, produces a force with contributions from the four components in Eq. (A5). Because p_∞ and $\bar{p}$ are constant, their surface integrals over S vanish. The resultant of p_u on S generates pressure drag. Although the latter vanishes on the entire RHB interface, it is finite on the frontal region,

$$\mathbf{F}_p \cdot \hat{\mathbf{x}} = \oint_S -p_u \hat{\mathbf{n}}\cdot\hat{\mathbf{x}}\mathrm{d}S, \tag{E6}$$

and consists of the forces $\mathbf{F}_\perp$, $\mathbf{F}_s$ and $\mathbf{F}_o$ exerted, respectively, on the exit plane, the interface, and a semi-circular region of infinitesimal radius around the source. Because $\theta_f > \pi/2$, the net pressure suction on the exit plane

$$\mathbf{F}_\perp \cdot \hat{\mathbf{x}} = -\left(\frac{\rho'}{2}U'^2 b' W\right)\left[(\pi-\theta_f)(2-\tan\theta_f/\theta_f)\right] < 0 \tag{E7}$$

resists frontal motion with a constant in brackets $\simeq 3.251$. To find $\mathbf{F}_s$, we calculate the outward normal projected along $\hat{\mathbf{x}}$

$$\hat{\mathbf{n}}\cdot\hat{\mathbf{x}} = \left\{1 + [(1/\tan\theta) - \theta/\sin^2\theta]^2\right\}^{-1/2}, \tag{E8}$$

and combine with curvilinear coordinate in Eq. (A2) and pressure in Eq. (B1). Then,

$$\mathbf{F}_s \cdot \hat{\mathbf{x}} = -\left(\frac{\rho'}{2}U'^2 b' W\right)\left[\frac{\sin^2\theta_f}{\theta_f}\right] < 0 \tag{E9}$$

resists frontal motion with a constant in brackets $\simeq 0.388$. Finally, at an arbitrary small radius around the source, pressure drag along $\hat{\mathbf{x}}$ is independent of such radius

$$\begin{aligned}\mathbf{F}_o \cdot \hat{\mathbf{x}} &= \frac{\rho'}{2}U'^2 b' W \int_{\theta=0}^{\pi}\left(2\cos\theta - \frac{b'}{r}\right)\cos\theta \mathrm{d}\theta \\ &= \pi\left(\frac{\rho'}{2}U'^2 b' W\right) > 0,\end{aligned} \tag{E10}$$

and thus it accelerates the front.

Before considering the remaining pressure p_z applied on S, we first evaluate momentum lost through surfaces of the frontal region. Because velocity is aligned with the boundary at the interface and snowpack surfaces, the only contributions to the surface integral in Eq. (31) are from the exit plane and the near vicinity of the source, where $\mathbf{u}_{\mathrm{rel}}\cdot\hat{\mathbf{n}}$ does not vanish. The resulting momentum loss produces an equal and opposite reaction force on the frontal region. On any small radius about the origin, $\mathrm{d}S = W r \mathrm{d}\theta$,

$\mathbf{u}' \cdot \hat{\mathbf{x}} = (b' \cos\theta/r - 1)$, and $\mathbf{u}_{\rm rel} \cdot \hat{\mathbf{n}} = U'(\cos\theta - b'/r)$, so the source momentum reaction force slows the frontal region,

$$\begin{aligned} \mathbf{M}_o \cdot \hat{\mathbf{x}} &= -\hat{\mathbf{x}} \cdot \int_{\theta=0}^{\pi} (\rho' \mathbf{u}')(\mathbf{u}_{\rm rel} \cdot \hat{\mathbf{n}}) \mathrm{d}S \\ &= -3\pi \left(\frac{\rho'}{2} U'^2 b' W \right) < 0. \end{aligned} \tag{E11}$$

In the quasi-steady approximation, the relative flow velocity at the exit plane with $\hat{\mathbf{n}} = -\hat{\mathbf{x}}$ is $\mathbf{u}_{\rm rel} = \mathbf{u}'$, so the corresponding momentum reaction force accelerates the frontal region,

$$\begin{aligned} \mathbf{M}_\perp \cdot \hat{\mathbf{x}} = -\int_{y=0}^{b'\theta_f} \rho' \left(\mathbf{u}' \cdot \hat{\mathbf{x}} \right) \left(\mathbf{u}_{\rm rel} \cdot \hat{\mathbf{n}} \right) W \mathrm{d}y = \\ \left(\frac{\rho'}{2} U'^2 b' W \right) \times \\ \Big[\frac{\sin^2\theta_f}{\theta_f} + 4\pi - 2\theta_f - (\pi - \theta_f) \frac{\tan\theta_f}{\theta_f} \Big], \end{aligned} \tag{E12}$$

where the constant in brackets is $\simeq 9.92$. As expected from potential flow theory, the total pressure drag from Eqs. (E9)-(E10) cancels the net reaction forces from Eq. (E11)–(E12). Finally, the projected buoyancy surface integral of p_z on S is, with $\hat{\mathbf{x}} \cdot \hat{\mathbf{z}} = -\sin\alpha$,

$$\mathbf{F}_b \cdot \hat{\mathbf{x}} = \oint_S -p_z \hat{\mathbf{n}} \cdot \hat{\mathbf{x}} \mathrm{d}S = a_V b'^2 W \rho' g \hat{\mathbf{z}} \cdot \hat{\mathbf{x}}. \tag{E13}$$

As expected from the divergence theorem, it cancels frontal weight along $\hat{\mathbf{x}}$,

$$\mathbf{F}_g \cdot \hat{\mathbf{x}} = a_V \rho' b'^2 W g \sin\alpha. \tag{E14}$$

Therefore, the resultant of all steady forces vanishes on the frontal region, leading to a paradox similar to *d'Alembert* [1752].

Appendix F: Resolution of d'Alembert's paradox

For boundary layers and wakes, *Prandtl* [1904] resolved d'Alembert's paradox by focusing on flow near solid walls and by introducing viscosity. Recently, *Hoffman and Johnson* [2010] did so while underlining the drawbacks of the inviscid Euler formulation; they indicated that the introduction of viscosity in the presence of slip degenerates into turbulence, thus producing substantial drag without the need to invoke a boundary layer. Unfortunately, flows possessing a turbulent wake cannot resolve d'Alembert's paradox *ab initio*, but must instead rely on empirical observations to some degree. In the cylinder wake, for instance, base suction pressure and vortex dynamics can be analyzed at low Reynolds number, but exhibit complex behavior at higher values, requiring experiments or numerical simulations to capture quantitatively [*Williamson*, 1996].

In this context, we now suggest how d'Alembert's paradox may be resolved to impart forward acceleration on a homogeneous frontal region. Within the control volume shaded in light grey in Fig. (1) of the paper, the actual static pressure field shares the same background p_∞, p_z and $\bar{p}$ as in Eqs. (A6) and (A7), but differs in its flow-induced pressure. Because the frontal region is subject to a vanishing net force in potential flow, any change from p_u in Eq. (A8) to the actual flow-induced pressure p_v results in a net longitudinal force on the frontal region

$$\mathbf{F}_A \cdot \hat{\mathbf{x}} = \oint_S (p_u - p_v) \hat{\mathbf{n}} \cdot \hat{\mathbf{x}} \mathrm{d}S. \tag{F1}$$

Using large-eddy-simulations (LES), *Carroll et al.* [2012] described how the flow in an eruption current differs from predictions of potential theory in Eq. (A3). They documented three changes suggesting a resolution of the paradox. As their animations available on line with *Phys. Fluids* revealed, these changes arose as soon as dynamic fluid viscosity μ_f was introduced with a source that was no longer infinitesimal, but instead possessed a uniform velocity profile on a finite radius.

First, stagnation expanded from a point into a well-mixed region of height h_s above the base. At relatively low Reynolds number $\mathrm{Re}_U \equiv \rho' U' b'/\mu_f$, *Carroll et al.* [2012] found

$$\frac{h_s}{b'} \simeq a_h \sqrt{\frac{1}{\mathrm{Re}_U}} \tag{F2}$$

with $a_h \simeq 54$, as theory would predict for a boundary layer growing forward from the source. For $\mathrm{Re}_U > 20,000$, the ratio appeared to asymptote to $h_s/b' \simeq 0.4$. Because the raised stagnation point belongs to the interface, its polar angle is $\theta_s = h_s/b'$. In such stagnated region, flow-induced pressure remains nearly equal to its value $p_{v_s} \sim p_{u_s}(\theta = 0) = (\rho'/2)U'^2$ along the interface in the range $0 < \theta < \theta_s$. Substituting in Eq. (F1) and integrating, the stagnated region generates a force slowing the frontal region,

$$\begin{aligned} \mathbf{F}_{A_S} \cdot \hat{\mathbf{x}} &= W \int_{\theta=0}^{\theta_s} [p_{u_s} - p_{u_s}(\theta = 0)] \mathrm{d}\theta \\ &= \left(\frac{\rho'}{2} U'^2 b' W \right) \left[\frac{\sin^2\theta_s}{\theta_s} - \theta_s \right] < 0. \end{aligned} \tag{F3}$$

However, at large Re_U with $\theta_s \simeq 0.4$, the constant in brackets is ~ -0.02, thus making this force contribute negligibly to frontal dynamics.

Second, although *Carroll et al.* [2012] observed large-scale fluctuations mixing slower ambient air through the interface, the resulting cloud deceleration amounted at worst to $< 24\%$ of pressure drag on the frontal region. Therefore, while air entrainment is necessary for the mass balance of air alone [*Louge et al.*, 2012], it should not matter to frontal dynamics.

Third, consistent with the region $(y > b' - x)$ of adverse streamwise pressure gradient predicted by potential flow theory, *Carroll et al.* [2012] found that the exit plane at $x = x_f$ is subject to a mixing recirculation resembling the wake behind a cylinder in cross-flow. For that classical problem, flow-induced pressure gradient along the interface of curvilinear coordinate s is first favorable $(\partial p_{u_s}/\partial s < 0)$ away from the stagnation point, and then it transitions to an adverse gradient $(\partial p_{u_s}/\partial s > 0)$, creating a recirculating wake with nearly equalized average flow-induced pressure, thus preventing recovery from the gradual pressure loss due to contraction of fluid streamlines upstream of separation [*Williamson*, 1996]. At the transition the cylinder has actual flow-induced suction pressure $p_v = \varpi p_u < 0$ with magnitude smaller than the potential flow theory prediction $p_u = -3\rho U^2/2$ by a factor $\varpi \simeq 0.84$ at large Reynolds number [*Achenbach*, 1968].

In static pressure records at the Vallée de la Sionne, *McElwaine and Turnbull* [2005] consistently observed that the loci of peak stagnation pressure and the downstream onset of vigorous pressure fluctuations were roughly equidistant from the point of minimum negative pressure. This suggests that the flow degenerated into strong mixing recirculation at a distance approximately b' behind the source. Such mixing likely weakened the flow-induced pressure that potential theory predicts at that point. In this context, it is reasonable to assume that suction on the exit plane of the frontal

region at $x = x_f \simeq -b'$ is reduced from its potential theory value by an amount $\varpi \simeq 0.84$ similar to that observed at the onset of the cylinder's wake, where pressure gradient also becomes adverse,

$$p_v = \varpi p_u < 0. \tag{F4}$$

Substituting this expression in Eq. (F1) and integrating p_u from Eq. (A8) across the exit plane with $\hat{\mathbf{n}} \cdot \hat{\mathbf{x}} = -1$, the corresponding deficit in suction force accelerates the frontal region

$$\mathbf{F}_{A_\perp} \cdot \hat{\mathbf{x}} = -(1-\varpi) \int_{y=0}^{b'\theta_f} p_u \mathrm{d}y = -(1-\varpi)\mathbf{F}_\perp \cdot \hat{\mathbf{x}} > 0, \tag{F5}$$

where $\mathbf{F}_\perp \cdot \hat{\mathbf{x}} < 0$ is given in Eq. (E7).

Without any substantial change to other forces predicted by potential theory in Eqs. (E9)–(E14), the resulting forward force may be cast in the formalism of Eq. (32) and, upon combining Eqs. (1), (2), (4), (5), (26), (E7) and (F5), we extract

$$\rho' \Gamma^* \sin\alpha = \rho \sin\alpha_{\text{eff}} \mathrm{Fr}^2/(1+\mathrm{Ri}), \tag{F6}$$

with effective inclination angle

$$\alpha_{\text{eff}} \equiv \arcsin\left[\pi \frac{(1-\varpi)}{a_V}(\pi - \theta_f)\left(2 - \frac{\tan\theta_f}{\theta_f}\right)\right]. \tag{F7}$$

With $\varpi = 0.84$, we find $\alpha_{\text{eff}} \simeq \pi/6$.

Appendix G: Longitudinal acceleration

We use Eq. (32) to estimate frontal acceleration from data of frontal height, speed, width and slope. First, we note that the difference between terms representing added mass and momentum relative to the source is small compared to the contribution of frontal speed to momentum of the frontal region. To show this, we write the term in square brackets in Eq. (33) as $\rho'(a_V b'^2 W)U(1+\Delta)$, where $\Delta \equiv [(a_\mu/a_V)(1-\zeta) - (a_M/a_V)\delta]$. Without a density difference between cloud and ambient air ($\zeta = 0, \delta = 1$), we find that $\Delta(\zeta = 0) = (a_\mu - a_M)/a_V \simeq 5.10^{-4}$ is small. At the first stable point, $\Delta(\zeta_e) = (1-2a_1)(a_\mu - a_M)/a_V$ is even smaller. Then, neglecting Δ, substituting Eqs. (5), (37), and (42), and approximating the mixed-mean density using Eq. (29), Eq. (32) yields a measurement of Γ^* that may be compared with predictions of Eq. (F6),

$$\Gamma^* \simeq \left(\frac{U^2}{g\tan\alpha}\right) \frac{\partial}{\partial x^*} \ln\left[\left(1 + \frac{U^2}{2gH'}\right) WUH'^2\right]. \tag{G1}$$

To estimate the derivative of the term in straight brackets without introducing excessive noise, we fit data for U, W [*Sovilla et al.*, 2006], and H' [*Vallet et al.*, 2004] using splines, differentiate the result, and present Γ^* at locations where primary data was reported. As Fig. 3 illustrates, despite inevitable noise, the measured relative acceleration is smaller than the prediction $\Gamma^* = \zeta$ for a solid object subject to classical weight and buoyancy forces, but is instead closer to the prediction of Eq. (F6).

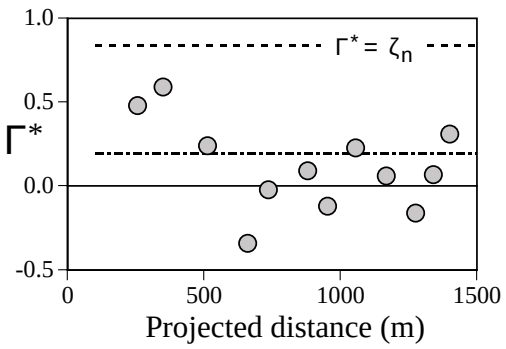

Figure 3. Relative acceleration Γ^* calculated using Eq. (G1) with field records of U, $\sin\alpha$ and W from *Sovilla et al.* [2006] and H' from *Vallet et al.* [2004] for avalanche 509 (symbols). The upper dashed line, which clearly overpredicts data, represents a model treating the frontal region as a solid object subject to weight and buoyancy, or $\Gamma^* = \zeta_n$. The lower dashed-dotted line is the prediction of Eq. (F6) $\simeq 0.194$ at the first stable state and average slope $\overline{\sin\alpha} \simeq 0.45$.

Appendix H: Impact pressure

Impact pressure is that which is exerted as a fluid is arrested by an obstacle in its path. Because it is dominated by fluid inertia, it is greater in the frontal region than outside, and it crucially depends on local density. Because our approach ignores stratification, it can only provide an estimate based upon mixed-mean density ρ'. However, the calculation is instructive in two ways. First, it reveals that impact pressure magnitude greatly exceeds static pressure calculated in Appendix A, thus underlying the fundamental difference between measurements of the former by *Sovilla et al.* [2008b] and of the latter by *McElwaine and Turnbull* [2005]. Second, it shows that reductions in impact pressure that are observed with increasing elevation above the snowpack are not proof that density alone decreases, but only that the combined product $\rho'\|\mathbf{u}' + U\hat{\mathbf{x}}\|^2$ does.

If the flow is arrested on quasi-steady local streamlines about the obstacle, and all energy is converted to impact pressure p_I irrespective of velocity direction, then

$$p'_I = p' + \frac{1}{2}\rho'\|\Delta\mathbf{u}\|^2, \tag{H1}$$

where p' is static pressure within the frontal region, and $\Delta\mathbf{u} \equiv \mathbf{u}' + U\hat{\mathbf{x}}$ is flow velocity relative to the obstacle. Impact is partially resisted by atmospheric pressure p_a exerted behind the obstacle or "stored" within it before the avalanche passed. To estimate the net force experienced by the obstacle, we subtract $p_a = p_\infty - \rho g z$ from p_I at the altitude $z = \sin\alpha(b' - x) + y\cos\alpha$ of a hit at (x, y) from the source. Using $\mathbf{u}'$ from Eq. (A4), p' from Eqs. (A5)-(A8), and frontal conditions from Eqs. (1)-(5), we find

$$\frac{p_I - p_a}{(\rho/2)U^2} = \left(\frac{\mathrm{Ri}}{1+\mathrm{Ri}}\right)\left(1 - \frac{z}{\pi b'}\right) + \left(\frac{1}{1-\zeta}\right)\left[(1-\delta)^2 + \frac{2xb'\delta}{x^2+y^2}\right]. \tag{H2}$$

The line $y = -x$ behind the source is the locus of impact pressure minima along the flow. Maxima occur ahead of the source where $y = x$,

$$\frac{(p_I - p_a)_{\max}}{(\rho/2)U^2} = \left(\frac{\mathrm{Ri}}{1+\mathrm{Ri}}\right)\left(1 - \frac{z}{\pi b'}\right) + \left(\frac{1}{1-\zeta}\right)\left[(1-\delta)^2 + \frac{b'\delta}{y}\right], \tag{H3}$$

reaching their smallest value on the interface where $y = \pi b'/4$. At that location, if $\alpha = 0$ and the avalanche has $\zeta = \zeta_n$ and $\mathrm{Ri} = \mathrm{Ri}_n$, the smallest peak impact pressure is

$(\rho U^2/2)[(4/\pi)+a1(3+2a_1)/2/(1-2a_1)] \simeq 6.3(\rho U^2/2)$. On the line of maximum impact pressure the resultant $\mathbf{u}'\cdot\hat{\mathbf{x}}+U$ exceeds frontal speed near the snowpack wherever $y < b'/2$. Therefore, peak impact pressure rises sharply toward the ground where the source augments frontal speed. Conversely, it drops above $y = b'/2$.

For avalanche 509, *Sovilla* [2012] shared impact pressure data with us for two pylon elevations at $y_p = 4.5\,\mathrm{m}$ and 5.5 m from hard ground. With snowpack depth $h_p \simeq 1.5\,\mathrm{m}$ estimated from the FMCW radar data of *Sovilla et al.* [2006], actual elevations are $y = y_p - h_p \simeq 3\,\mathrm{m}$ and 4 m above the snow cover. Adopting our prediction for H' in section (8), we estimate $b'\delta \simeq 1.5\,\mathrm{m}$. With operations at (Ri_n, ζ_n), and our prediction for U at the pylon, Eq. (H3) yields $(p_I - p_a)_{\max} \simeq 16\,\mathrm{kPa}$ and $\simeq 14\,\mathrm{kPa}$ at $y \simeq 3\,\mathrm{m}$ and 4 m, respectively, while *Sovilla* [2012] recorded $(p_I - p_a)_{\max} \simeq 50\,\mathrm{kPa}$ and $\simeq 20\,\mathrm{kPa}$. Although our estimates have the right order of magnitude, the data suggest that the flow is stratified.

Notation

a_0, a_1, κ	exact fluidization constants.
a_V, a_M, a_μ	exact constants in App. E.
a_A, a_R, a_X	exact constants.
b'	source to stagnation distance.
$\mathbf{F}_A$, $\mathbf{F}_{A_s}$, $\mathbf{F}_{A_\perp}$	resultant forces in App. F.
$\mathbf{F}_\perp$	drag on exit plane.
$\mathbf{F}_b$	buoyancy force.
Fr	Froude number in Eq. (26).
g	gravity.
h'	snowpack fluidization depth.
H'	asymptotic cloud height.
ℓ	spreading length in Eq. (43).
$\dot{m}_a$	air entrainment rate.
$\dot{m}_e$	frontal output mass flow rate.
$\dot{m}_s$	source mass flow rate.
$\hat{\mathbf{n}}$	outward unit vector.
p'	static pressure.
p_I	impact pressure.
p_u	potential-flow-induced pressure.
p_v	actual flow-induced pressure.
p_z	hydrostatic pressure component.
r, θ	polar coordinates.
Ri	Richardson number in Eq. (3).
U	frontal speed.
U'	source fluid asymptotic speed
$\mathbb{V}_T$	total avalanche volume.
W	cloud width.
$\hat{\mathbf{x}}$	unit vector along the slope.
$\hat{\mathbf{y}}$	unit vector $\perp$ snowpack.
$\hat{\mathbf{z}}$	upward unit vertical.
α	slope angle.
Γ^*	relative acceleration in Eq. (32).
δ	swelling ratio in Eq. (1).
ζ	relative density in Eq. (2).
κ_0	ignition parameter in Eq. (12).
λ	scoured snowpack fraction.
μ_e	effective snowpack friction.
ϖ	suction deficit in Eq. (F4).
ρ'	frontal mixed-mean density.
ρ, ρ_c	air and snowpack densities.

References

Achenbach, E. (1968), Distribution of local pressure and skin friction around a circular cylinder in cross-flow up to $\mathrm{Re} = 5\times10^6$, *J. Fluid Mech.*, *34*, 625–639.

Carroll, C. S., B. Turnbull, and M. Y. Louge (2012), Role of fluid density in shaping eruption currents driven by frontal particle blowout, *Phys. Fluids*, *24*, 066603.

d'Alembert, J. le Rond. (1752), *Essai d'une nouvelle théorie de la résistance des fluides*, Paris.

Hoffman, J., and C. Johnson (2010), Resolution of d'Alembert's paradox, *J. Math. Fluid Mech.*, *12*, 321–334.

Kays, W. M., M. R. Crawford, and B. Weigand (2005), *Convective Heat and Mass Transfer, 4th Edition*, McGraw-Hill, NY, USA.

Louge, M. Y., C. S. Carroll, and B. Turnbull (2012), Reply to comment by P. A. Bartelt and O. Buser on "Role of pore pressure gradients in sustaining frontal particle entrainment in eruption currents: The case of powder snow avalanches", *J. Geophys. Res.*, *117*, F02016, doi:10.1029/2012JF002380.

McElwaine, J. N., and B. Turnbull (2005), Air pressure data from the Vallée de la Sionne avalanches of 2004, *J. Geophys. Res.*, *110*, F03010, doi:10.1029/2004JF000237.

Prandtl, L. (1904), Über Flussigkeitsbewegung bei sehr kleiner Reibung (On motion of fluids with very little viscosity), *Third International Congress of Mathematics, Heidelberg*, `http://naca.larc.nasa.gov/digidoc/report/tm/52/NACA-TM-452.PDF`

Sovilla, B. (2012), *Personal communication.*

Sovilla, B., P. Burlando, and P. Bartelt (2006), Field experiments and numerical modeling of mass entrainment in snow avalanches, *J. Geophys. Res.*, *111*, F03007, doi: 10.1029/2005JF000391.

Sovilla, B., M. Schaer, and L. Rammer (2008b), Measurements and analysis of full-scale avalanche impact pressure at the Vallée de la Sionne test site, *Cold Reg. Sci. Tech.*, *51*, 122–137.

Strehlow, R. (1984), *Combustion Fundamentals*, McGraw-Hill, NY.

Turnbull, B., and J. N. McElwaine (2007), A comparison of powder-snow avalanches at Vallée de la Sionne, Switzerland, with plume theories, *J. Glaciol.*, *53*, 30–40.

Uppal, A., W. H. Ray, and A. B. Poore (1976), The classification of the dynamic behavior of continuous stirred tank reactors – influence of reactor residence time, *Chem. Eng. Sci.*, *31*, 205–214.

Vallet, J., B. Turnbull, S. Joly, and F. Dufour (2004), Observations on powder snow avalanches using videogrammetry, *Cold Reg. Sci. Tech.*, *39*, 153–159.

Williamson, C. H. K. (1996), Vortex dynamics in the cylinder wake, *Ann. Rev. Fluid Mech.*, *28*, 477–539.

C. S. Carroll, Sibley School of Mechanical and Aerospace Engineering, Cornell University, Ithaca, NY 14853, USA. (CSC92@cornell.edu)

M. Y. Louge, Sibley School of Mechanical and Aerospace Engineering, Cornell University, Ithaca, NY 14853, USA. (MYL3@cornell.edu)

B. Turnbull, Division of Process and Environmental Engineering, University of Nottingham Nottingham, UK NG7 2RD. (barbara.turnbull@nottingham.ac.uk)